RSC Advances

PAPER

View Article Online
View Journal | View Issue

Cite this: *RSC Adv.*, 2025, **15**, 3080

Study of nitrous oxide utilization for syngas production *via* partial oxidation of methane using Ni-doped perovskite catalysts

Notsawan Swadchaipong,[a] Vut Tongnan,[a] Panupan Maneesard,[a] Matthew Hartley,[b] Kang Li,[c] Rossarin Ampairojanawong,[a] Ammarika Makdee,[a] Unalome Wetwatana Hartley[a] and Issara Sereewatthanawut*[de]

Four different materials—pure NiO, pure LSCF ($La_{0.3}Sr_{0.7}Co_{0.7}Fe_{0.3}O_{3-\delta}$), 10% Ni/LSCF, and 20% Ni/LSCF—were studied. The Ni/LSCF catalysts demonstrated superior catalytic performance for both N_2O decomposition and the partial oxidation of methane (POM) compared to pure NiO and pure LSCF. This enhancement is attributed to an increase in oxygen vacancies and improved oxygen mobility within the catalyst, as evidenced by O_2-TPD analysis. During N_2O decomposition, both LSCF and 10% Ni/LSCF achieved complete N_2O conversion at 800 °C, whereas pure NiO provided 81.7% at the same temperature. However, 10% Ni/LSCF is more active at lower temperatures, as evidenced by its T_{50} value of 536 °C, compared to 546 °C for the unmodified LSCF. For the POM reaction using N_2O as an oxidant, 10% Ni/LSCF achieved 70.9% CH_4 conversion, 96.6% CO selectivity, and 97.4% H_2 selectivity at 600 °C. In contrast, both pure LSCF and 20% Ni/LSCF catalysts exhibited significantly lower efficiency, with approximately 20% CH_4 conversion and less than 5% syngas selectivity. The enhanced performance of the 10% Ni/LSCF compared to the 20% Ni/LSCF is likely attributed to its smaller Ni crystallite size (23.7 nm *vs.* 32.3 nm) and the lower temperature required for reducing Ni^{2+} to the active Ni^0 species (480 °C *vs.* 500 °C). Kinetic analysis of the POM reaction using N_2O over the 10% Ni/LSCF catalyst revealed a second-order reaction with respect to CH_4 and a zero-order reaction with respect to N_2O, with an apparent activation energy of 71.8 kJ mol^{-1}.

Received 21st September 2024
Accepted 20th January 2025

DOI: 10.1039/d4ra06805j

rsc.li/rsc-advances

1. Introduction

One of humanity's greatest concerns is global warming, driven by the emission of greenhouse gases (GHGs) such as carbon monoxide (CO), carbon dioxide (CO_2), methane (CH_4), and nitrous oxide (N_2O). Nitrous oxide and methane are significantly more potent than CO_2 in terms of global warming potential over a 100 year period, with N_2O being approximately 310 times and CH_4 being about 21 times more harmful.[1–4] Since the Industrial Revolution, atmospheric N_2O concentrations have increased due to human activities such as agricultural emissions, biomass burning, fossil fuel combustion, and industrial activities in which N_2O is an undesirable byproduct of chemical processes such as adipic acid and nitric acid production.[5,6] To address the issues caused by N_2O, two main strategies are employed: (i) reducing its formation and (ii) implementing post-treatment technologies to mitigate its emission.[5] Several post-treatment technologies have been developed to control N_2O emissions in the chemical and energy industries, including thermal decomposition, non-selective catalytic reduction (NSCR), selective catalytic reduction (SCR), and direct catalytic decomposition.[7–10] Among these, the catalytic decomposition of N_2O into N_2 and O_2, as illustrated in eqn (1), is particularly attractive due to its simplicity, high efficiency, low cost, and minimal energy requirements.[11] In contrast, CH_4 emissions primarily originate from agriculture, fossil fuel extraction, and landfill waste decomposition. CH_4 can be utilized as an energy source or converted into valuable chemicals such as methanol, liquid fuels and ammonia. This study focused on utilizing N_2O and CH_4 in a single process. The N_2O will be employed as an oxidant, resulting in a synergy of N_2O decomposition and syngas production *via* partial methane oxidation (POM). While N_2O supply is limited compared to natural gas, substantial amounts of N_2O are found as a byproduct of the industrial sector in concentrations acceptable to be utilized as an oxidant.[12] This process offers the

[a]*Chemical and Process Engineering, The Sirindhorn International Thai-German Graduate School of Engineering (TGGS), King Mongkut's University of Technology North Bangkok, Bangkok, 10800, Thailand. E-mail: unalome.w.cpe@tggs-bangkok.org*

[b]*Chemical Engineering, Engineering Faculty, King Mongkut's University of Technology North Bangkok, Bangkok, 10800, Thailand*

[c]*Chemical Engineering, Imperial College London, London, SW7 2AZ, UK*

[d]*King Prajadhipok's Institute, Bangkok 10210, Thailand*

[e]*Faculty of Engineering and Technology, Pathumthani University, Pathumthani 12000, Thailand. E-mail: issara.se@kpi.ac.th*

advantage of operating at lower temperatures while producing a more valuable product: syngas, a mixture of H_2 and CO, as shown in eqn (2) and (3).

$$2N_2O \rightarrow 2N_2 + O_2,\ \Delta H_{298K} = -163\ \text{kJ mol}^{-1} \quad (1)$$

$$CH_4 + 1/2O_2 \rightarrow CO + 2H_2,\ \Delta H_{298K} = -36\ \text{kJ mol}^{-1} \quad (2)$$

$$N_2O + CH_4 \rightarrow N_2 + CO + 2H_2,\ \Delta H_{298K} = -118\ \text{kJ mol}^{-1} \quad (3)$$

In this process, N_2O decomposes at oxygen vacancy sites (*) on the catalyst surface, forming adsorbed oxygen (O*) (eqn (4)). This adsorbed oxygen then oxidizes CH_4, producing syngas and regenerating oxygen vacancies, as described in eqn (5).

$$N_2O + * \rightarrow N_2 + O* \quad (4)$$

$$O* + CH_4 \rightarrow CO + 2H_2 + * \quad (5)$$

Perovskite materials are well-known in catalysis for their excellent oxygen mobility, redox properties, and thermal stability. These characteristics make them ideal for supporting the above reactions which require efficient oxygen exchange and high thermal resistance. The catalytic performance of perovskites can be further optimized through the partial substitution of A- and B-site cations with different valence states $A_xA'_{x-1}B_yB'_{y-1}O_{3-\delta}$, where δ denotes the concentration of oxygen vacancies). This substitution allows for the fine-tuning of surface and redox properties, thereby enhancing catalytic activity.[13–16] For instance, K. L. Pan *et al.*[17] found that partially substituting La in La_2NiO_4 with Sr and Ce significantly enhanced catalytic performance for the N_2O decomposition, enabling $La_{0.7}Ce_{0.3}SrNiO_4$ to achieve 100% N_2O conversion at 600 °C with long-term stability of 60 h. C. Huang *et al.*[18] observed that replacing some Fe in $BaFeO_{3-\delta}$ with Sn increased oxygen mobility and decreased the activation energy for the N_2O decomposition. In the partial oxidation of CH_4, the substitution of Ni with Co ($LaNi_{0.8}Co_{0.2}O_3$) resulted in higher activity and reduced coke deposition.[19]

Among perovskite materials, $La_xSr_{x-1}Co_yFe_{y-1}O_{3-\delta}$ has attracted significant attention as a potential catalyst for the N_2O decomposition and partial oxidation of CH_4 reactions due to its high catalytic activity and chemical and thermal stability.[15,20,21] Adding Sr and Fe to the $LaCoO_3$ structure increased the weakly adsorbed oxygen, which is crucial for improving catalytic properties.[22] In this study, $La_{0.3}Sr_{0.7}Co_{0.7}Fe_{0.3}O_{3-\delta}$ (LSCF3773) was selected due to its superior redox properties, as indicated by significant changes in oxygen non-stoichiometry ($\Delta\delta_3$) of 0.40 compared to other compositions.[23] The incorporation of metal oxides, such as NiO, into promising perovskite structures can further enhance the overall catalytic performance. This modification improves key properties like oxygen mobility, redox activity, and stability, making the catalyst more effective for the combined reaction. Ni-based catalysts have been widely used in CH_4 oxidation reactions due to their high activity for C–H bond cleavage, excellent oxygen transfer capacity, and ability to support heat-resistant oxides, thus, enhancing thermal stability.[24] K. Takehira *et al.*[25] observed that incorporating Ni into perovskites ($SrTiO_3$, $BaTiO_3$, and $CaTiO_3$) increased POM activity and inhibited Ni coking on the catalyst due to finely dispersed nickel metal particles and partly assisted by the mobile oxygen on the catalyst. Likewise, the effect of Ni addition on the POM activity of perovskite material was also investigated by X. Yin and co-workers.[26] They concluded that Ni doping activates methane molecules and increases oxygen vacancies on the surface of $LaMnO_{3+\delta}$ perovskite, leading to improved performance in the POM reaction with high methane conversion, syngas selectivity, and yield. Ni metal has also been selected for large-scale applications due to its abundance and cost-effectiveness.[14]

This study investigated catalytic performance of synthesized Ni/LSCFs towards the POM using N_2O as an oxidant. X-ray diffraction (XRD), H_2-temperature programmed reduction (H_2-TPR), CH_4-temperature programmed surface reaction (CH_4-TPSR), and O_2-temperature programmed desorption (O_2-TPD) techniques were employed to characterize the catalysts' properties. Catalytic performances were evaluated in a packed-bed reactor, focusing on the effects of reaction temperature and Ni loading on catalytic performance. Kinetic parameters such as the reaction rate, rate constant, reaction order, and activation energy were also examined.

2. Experiment

2.1 Synthesis of LSCF

The LSCF perovskite was synthesized using a modified Pechini method, with EDTA and citric acid serving as chelating agents (citrate-EDTA complexing method).[27,28] In this process, all metal nitrate precursors, including lanthanum(III) nitrate nonahydrate ($La(NO_3)_3\cdot 9H_2O$), strontium nitrate ($Sr(NO_3)_2$), cobalt(II) nitrate hexahydrate ($Co(NO_3)_2\cdot 6H_2O$) and iron(III) nitrate nonahydrate ($Fe(NO_3)_3\cdot 9H_2O$) were dissolved and mixed in 100 mL of deionized water. Separately, ethylenediaminetetraacetic acid (EDTA) was dissolved in a solution of 28–30% w/w ammonium hydroxide (NH_4OH) and then diluted with deionized water. The EDTA solution was slowly added to the metal nitrate solution using a syringe pump, with continuous stirring to form a metal-EDTA complex. Citric acid monohydrate (CA) was then added to create a metal-EDTA-CA complex which was then polymerized by adding ethylene glycol (EG). The molar ratio of total metal cations: EDTA : CA : EG was maintained at 1 : 1:1.5 : 1. The pH of the polymerized complex was adjusted to 6–7 using NH_4OH and stirred continuously at 80–90 °C until a dark brown gel formed. The resulting gel was dried overnight at 150 °C in a vacuum oven, obtaining a foam-like powder. The powder was further ground and calcined in air at 1100 °C with a heating rate of 2 °C min^{-1} for 12 h, giving the complete perovskite phase.

2.2 Ni impregnation

Ni/LSCF catalysts with 10 and 20%Ni loading were synthesized *via* the wet impregnation method using nickel(II) nitrate hexahydrate ($Ni(NO_3)_2\cdot 6H_2O$) as the Ni source. The Ni precursor, corresponding to 10 or 20%Ni, was dissolved in deionized water

and then mixed with the as-synthesized LSCF powder under continuous stirring at room temperature for 2 h. The mixture was dried overnight at 120 °C, followed by calcination at 700 °C with a heating rate of 10 °C min^{-1} for 12 h.

2.3 Characterizations

The crystalline structure of the catalysts was examined using X-ray diffraction (XRD) on a Bruker AXS D8 diffractometer with Cu K_α radiation (λ = 1.5410 Å) over a scan range of 20 to 80° at a scan speed of 0.02° s^{-1}. Crystallite size was calculated using Scherrer's equation, based on the main reflection peaks in the XRD patterns.

Catalyst reducibility was evaluated by H_2-temperature programmed reduction (H_2-TPR), where 1.0 g of the catalyst was placed into a quartz tube reactor. The sample was pretreated at 700 °C for 1 h with 100 mL min^{-1} of 10% O_2/Ar to eliminate surface impurities. After cooling to room temperature under Ar flow, 100 mL min^{-1} of 5% H_2/Ar was introduced, and the temperature was increased from 25 to 950 °C at a heating rate of 5 °C min^{-1}. The H_2 consumption was analyzed using an on-line mass spectrometer (GSD 320, OmniStar).

The interaction of CH_4 with the catalyst surface and the formation of product gases during CH_4 oxidation were investigated using CH_4-temperature programmed surface reaction (CH_4-TPSR) on the same instrument as the H_2-TPR. After pretreatment with 10% H_2/Ar at 500 °C for 2 h and cooling to room temperature under Ar flow, 100 mL min^{-1} of 5% CH_4/Ar was introduced with temperature increasing from 25 to 950 °C (5 °C min^{-1}). An on-line mass spectrometer (GSD 320, OmniStar) was employed to detect effluent gases during the process.

Oxygen vacancies and mobility in the catalyst were investigated using O_2-temperature programmed desorption (O_2-TPD) on the same equipment as the H_2-TPR. The sample was first treated with 100 mL min^{-1} of 10% O_2/Ar at 700 °C for 1 h. After cooling to room temperature in an oxygen atmosphere, the sample was flushed with Ar and the temperature was increased to 950 °C at 5 °C min^{-1}. The oxygen desorption amount was continuously monitored using an on-line mass spectrometer (GSD 320, OmniStar).

2.4 Catalytic activity tests

2.4.1 Catalytic N_2O decomposition. The catalyst (2.0 g) was pelletized, sieved to a particle size of 0.075–0.18 mm, and placed into a quartz tube reactor supported by quartz wool plugs. The reactions were conducted in a packed-bed reactor. The catalyst bed was pretreated at 700 °C with 10% O_2/Ar to remove carbonaceous residues, then cooled to 500 °C under 100 mL min^{-1} of Ar. After that, 100 mL min^{-1} of 15% N_2O/Ar (WHSV = 3000 mL g_{cat}^{-1} h^{-1}) was introduced, and the temperature was linearly increased to 900 °C. Gaseous products were analyzed using a Shimadzu GC-2014ATF gas chromatograph equipped with a thermal conductivity detector (TCD) and a Molecular sieve 13X (MS-13X), Porapak N, and Q packed columns. N_2O conversion and products (N_2 and O_2) selectivity were calculated using eqn (6)–(8):

$$N_2O\ \text{conversion}(\%) = \left(\frac{F^{in}_{N_2O} - F^{out}_{N_2O}}{F^{in}_{N_2O}}\right) \times 100 \quad (6)$$

$$N_2\ \text{selectivity}(\%) = \left(\frac{F_{N_2}}{F^{in}_{N_2O} - F^{out}_{N_2O}}\right) \times 100 \quad (7)$$

$$O_2\ \text{selectivity}(\%) = \left(\frac{2 \times F_{O_2}}{F^{in}_{N_2O} - F^{out}_{N_2O}}\right) \times 100 \quad (8)$$

where $F^{in}_{N_2O}$ denotes the molar flow rate of N_2O in the feed stream. $F^{out}_{N_2O}$ F_{N_2}, and F_{O_2} represent the molar flow rates of N_2O, N_2, and O_2 in the outlet stream, respectively.

2.4.2 Partial oxidation of CH_4 (POM) using N_2O as an oxidant. The catalyst (2.0 g, particle size of 0.075–0.18 mm) was placed into a quartz tube packed-bed reactor. The catalyst was pretreated with 10% H_2/Ar at 500 °C for 2 h, then purged with Ar at the same temperature. The mixture of CH_4 and N_2O (molar ratio of $CH_4 : N_2O = 1 : 1$) was then introduced into the reactor (WHSV = 3000 mL g_{cat} h^{-1}) at atmospheric pressure. The temperature was gradually increased from 500 to 900 °C. The gases exiting the reactor were passed through a cold trap and continuously analyzed using a Shimadzu GC-2014ATP gas chromatograph equipped with a thermal conductivity detector (TCD) and a Molecular sieve 13X (MS-13x), Porapak N and Q packed columns. The conversion of CH_4, selectivity of products (H_2, CO, and CO_2) and H_2/CO molar ratio were calculated using eqn (9)–(13):

$$CH_4\ \text{conversion}(\%) = \left(\frac{F^{in}_{CH_4} - F^{out}_{CH_4}}{F^{in}_{CH_4}}\right) \times 100 \quad (9)$$

$$H_2\ \text{selectivity}(\%) = \left(\frac{F_{H_2}}{2\left(F^{in}_{CH_4} - F^{out}_{CH_4}\right)}\right) \times 100 \quad (10)$$

$$CO\ \text{selectivity}(\%) = \left(\frac{F_{CO}}{\left(F^{in}_{CH_4} - F^{out}_{CH_4}\right)}\right) \times 100 \quad (11)$$

$$CO_2\ \text{selectivity}\ (\%) = (100 - S_{CO}) \times 100 \quad (12)$$

$$\frac{H_2}{CO}\ \text{molar ratio} = \frac{F_{H_2}}{F_{CO}} \quad (13)$$

where $F^{in}_{CH_4}$ represents the molar flow rate of CH_4 in the feed stream. $F^{out}_{CH_4}$, F_{H_2}, and F_{CO} denote the molar flow rates of CH_4, H_2, and CO in the outlet stream, respectively.

3. Results and discussion

3.1 Characterizations

3.1.1 X-ray diffraction (XRD) analysis. The crystalline structures of the catalysts were characterized using X-ray diffraction (XRD). The XRD patterns of pure NiO exhibited diffraction peaks at 37.3°, 43.4°, 62.9°, 75.5°, and 80.2°, corresponding to the (111), (200), (220), (311), and (222) planes of the cubic NiO structure (PDF card no. 03-065-5745), as shown in

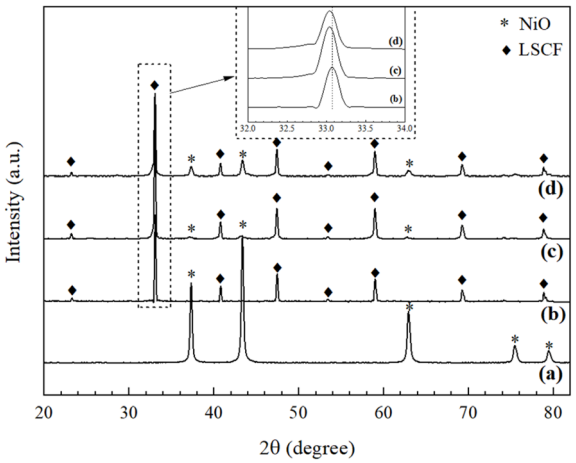

Fig. 1 XRD patterns and magnification of LSCF peak at 33.1° (inset) for (a) pure NiO, (b) LSCF, (c) 10% Ni/LSCF, and (d) 20% Ni/LSCF.

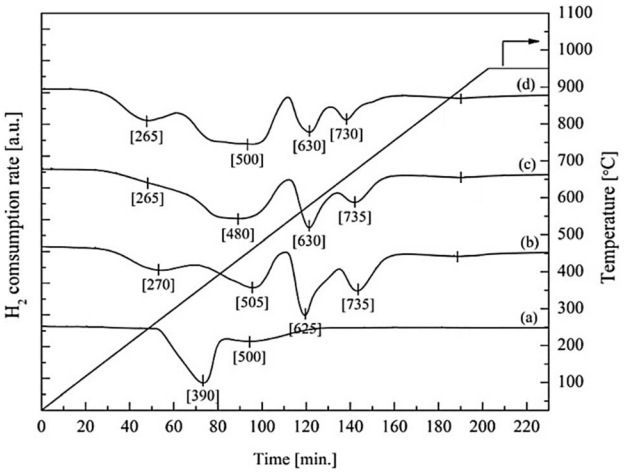

Fig. 2 H_2-TPR profiles of (a) pure NiO, (b) LSCF, (c) 10% Ni/LSCF, and (d) 20% Ni/LSCF.

Fig. 1(a). Fig. 1(b) shows the XRD pattern of LSCF at diffraction peaks of 23.3°, 33.1°, 40.8°, 47.4°, 53.4°, 59.0°, 69.3°, and 78.9°, which correspond to the (012), (110), (202), (024), (122), (214), (208), and (128) planes of the cubic structure of perovskite (PDF card no. 08-6122). The absence of impurity peaks in the XRD patterns of LSCF suggests that a single-phase perovskite structure was formed during the synthesis process. Fig. 1(c) and (d) illustrate the XRD patterns of Ni-doped LSCF catalysts that contain peaks from both the LSCF and NiO phases. The addition of Ni resulted in a slight shift of the LSCF peak to a lower 2θ value, as seen in Fig. 1(inset). This shift is attributed to the incorporation of Ni inside the LSCF structure, leading to its lattice expansion.[29] Furthermore, the presence of the NiO diffraction peak suggests that an excess amount of added Ni was crystallized on the LSCF surface. The intensity of the NiO diffraction peak increased with increasing Ni levels, indicating enhanced crystallinity and crystallite size of the NiO phase, with the NiO crystallite size in 20% Ni/LSCF (32.3 nm) being larger than in 10% Ni/LSCF (23.7 nm).

3.1.2 H_2-temperature programmed reduction (H_2-TPR) analysis. The reducibility properties of the catalysts were evaluated using H_2-temperature programmed reduction (H_2-TPR). The H_2-TPR profile of pure NiO (Fig. 2(a)) showed two reduction peaks at 390 and 500 °C, corresponding to the reduction of NiO on the surface and in bulk to metallic Ni, respectively.[30] The H_2-TPR profile of the LSCF catalyst (Fig. 2(b)) exhibited four reduction peaks. The reduction peak at 270 °C is attributed to the reduction of surface oxygen.[31] The peaks at 505, 625, and 735 °C correspond to a three-stage reduction process: (i) Co^{3+} to Co^{2+} and Fe^{4+}/Fe^{5+} to Fe^{3+}, (ii) Co^{2+} to Co^0 and Fe^{3+} to Fe^{2+}, and (iii) Fe^{2+} to Fe^0, respectively.[32] For Ni-doped LSCF catalysts, the H_2-TPR profiles (Fig. 2(c) and (d)) were similar to those of LSCF rather than pure NiO, indicating that the Ni content was insufficient to significantly impact the crystal structure.[33–36] However, the Ni-doped LSCF exhibited a broader reduction peak around 500 °C compared to pure LSCF, which is due to the overlapping reduction of Ni^{2+} to Ni^0, Co^{3+} to Co^{2+}, and Fe^{4+}/Fe^{5+} to Fe^{3+}. The shift in the reduction peak from 480 to 500 °C with increasing Ni loading from 10 to 20% is likely attributed to the larger NiO crystallite size, making the reduction of bulk NiO more difficult. R.K. Singha *et al.*[34] reported that the core structure of NiO could not be fully exposed to H_2 during TPR analysis, requiring longer times and higher temperatures for effective reduction. The H_2-TPR analysis revealed that the temperature of 500 °C was sufficient to reduce NiO to metallic Ni, which is the active species for the partial oxidation of CH_4 reaction.

3.1.3 CH_4-temperature programmed surface reaction (CH_4-TPSR) analysis. The CH_4-temperature programmed surface reaction (CH_4-TPSR) technique was performed to examine CH_4 dissociation and oxidation at active sites on the catalyst surface in the absence of gaseous oxygen. Despite the lack of oxygen, CH_4 could still be oxidized by interacting with the oxygen-enriched surface of the catalyst, producing H_2, CO, and CO_2. The 10% Ni/LSCF catalyst was selected as a representative sample for the CH_4-TPSR analysis and the results are reported in previous work.[37] The CH_4-TPSR analysis revealed that the 10% Ni/LSCF catalyst effectively functioned as an oxygen carrier, exhibiting significant oxidative properties, particularly in the 600–900 °C range. This temperature range was identified as the optimal condition for investigating the catalytic behavior of the as-synthesized catalyst for the CH_4 partial oxidation in this work.

3.1.4 O_2-temperature programmed desorption (O_2-TPD) analysis. The oxygen vacancies and mobility within the as-synthesized catalysts were investigated using the O_2-TPD technique, which measures the amount of oxygen desorbed from the catalyst surface after adsorption at 700 °C. Fig. 3 shows the O_2-TPD profiles of pure NiO, LSCF, 10% Ni/LSCF, and 20% Ni/LSCF catalysts. Unlike the NiO catalyst, where oxygen desorption peaks were difficult to observe, the LSCF-based catalysts displayed two distinct peaks. The first broad peak at around 400 °C is attributed to suprafacial oxygen (O_2^-, O_2^{2-} and O^-) adsorbed on oxygen vacancies, which readily desorb from the surface and play a crucial role in CH_4 partial oxidation. The shift of this peak to lower temperatures with increasing Ni content

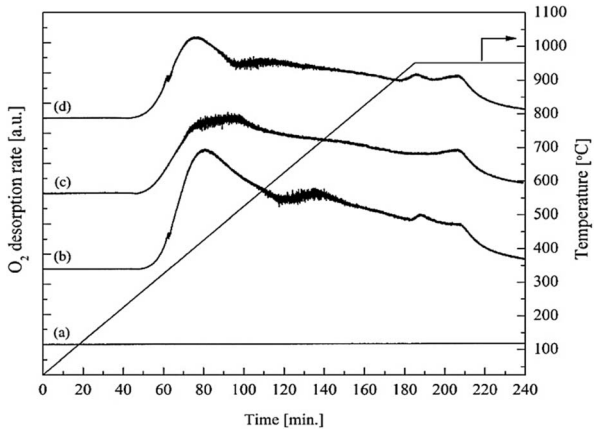

Fig. 3 O_2-TPD profiles of (a) pure NiO, (b) LSCF, (c) 10% Ni/LSCF, and (d) 20% Ni/LSCF.

suggests easier oxygen desorption from the surface, indicating that Ni addition into the LSCF enhances oxygen mobility within the catalyst. The second peak at around 950 °C corresponds to intrafacial oxygen (O^- and O^{2-}) within the bulk lattice of LSCF.[38]

3.2 Catalytic performances

3.2.1 Catalytic N_2O decomposition. The catalytic performance of the as-synthesized catalysts for the N_2O decomposition reaction is revealed in Fig. 4. Fig. 4(a) shows the N_2O conversion of NiO, LSCF, and 10% Ni/LSCF catalysts as a function of operating temperature. As the temperatures increased from 500 to 700 °C, N_2O conversion increased dramatically: from 24.7% to 70.8% for NiO, 20.3% to 98.2% for LSCF, and 20.0% to 99.7% for 10% Ni/LSCF. This enhancement is attributed to the increased thermal energy overcoming the activation energy of the reaction. Although N_2O decomposition is an exothermic reaction ($\Delta H_{298K} = -163$ kJ mol^{-1}), high temperatures are required to address kinetic limitations. At 800 °C, the LSCF-based catalysts achieved 100% N_2O conversion, while NiO reached only 81.7%. This suggests that LSCF-based catalysts are more effective than NiO, likely due to their superior oxygen vacancies and improved oxygen mobility, as indicated by O_2-TPD. The incorporation of Ni into LSCF further enhanced oxygen mobility and catalytic activity. This enhancement is reflected in the T_{50} values, which represent the temperature required for 50% N_2O conversion, with T_{50} values of 535.9 °C for the 10% Ni/LSCF and 545.7 °C for LSCF.

Our previous studies have highlighted the crucial role of oxygen vacancies and mobility in perovskite catalysts for efficient N_2O decomposition.[39] The N_2O decomposition mechanism begins with N_2O adsorption at oxygen vacancy sites (*) on the catalyst surface, followed by decomposition into N_2 gas and adsorbed oxygen (O*). The adsorbed oxygen can either react with another N_2O molecule to produce N_2 and O_2 or combine with another adsorbed oxygen to form O_2. These processes are represented by eqn (14)–(16).

$$N_2O + * \rightarrow N_2 + O* \quad (14)$$

$$N_2O + O* \rightarrow N_2 + O_2 + * \quad (15)$$

$$2O* \rightarrow O_2 + 2* \quad (16)$$

Fig. 4(b) shows that the N_2 and O_2 selectivity remained above 99% within the temperature range of 500–800 °C for all catalysts. However, at 900 °C, N_2 selectivity slightly decreased to 98.9, 98.2, and 96.8%, while O_2 selectivity dropped to 92.4, 94.0, and 91.2% for NiO, LSCF, and 10% Ni/LSCF, respectively. This decline is likely due to the formation of nitrogen dioxide (NO_2) as a by-product.[40] According to M. Shelef and G.W. Graham,[41] the produced adsorbed oxygen (as described in eqn (14)) may react with N_2O to generate nitric oxide (NO) (eqn (17)). The produced NO then combines with the adsorbed oxygen, forming NO_2 (eqn (18)).

$$N_2O + O* \rightarrow 2NO + * \quad (17)$$

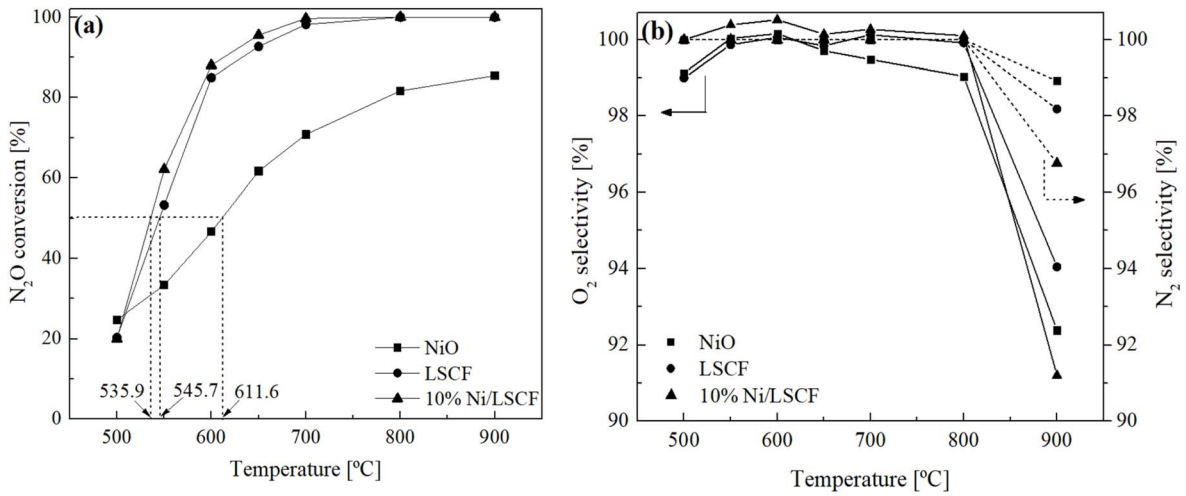

Fig. 4 Catalytic performance of NiO, LSCF, and 10% Ni/LSCF catalysts in terms of (a) N_2O conversion and (b) products (N_2 and O_2) selectivity as a function of temperature for the catalytic N_2O decomposition (15% N_2O/Ar, WHSV = 3000 mL g_{cat} h^{-1}, atmospheric pressure).

$$NO + O^* \rightarrow NO_2 + * \quad (18)$$

3.2.2 Partial oxidation of CH_4 (POM) using N_2O as an oxidant. This section investigates the effects of reaction temperature and Ni loading on the catalytic performance and reaction pathways of the as-synthesized catalysts for the partial oxidation of CH_4 using N_2O as the oxidant. The mechanisms of this reaction involve (i) the decomposition of N_2O to produce the adsorbed oxygen, as previously mentioned, and (ii) the partial oxidation of CH_4 using the adsorbed oxygen produced by N_2O decomposition, which will be further discussed. Before testing, the catalysts were pretreated at 500 °C for 2 h in an H_2/Ar atmosphere to reduce Ni^{2+} to the active Ni^0 species for the POM reaction. Furthermore, kinetic parameters such as reaction rate, reaction order, and activation energy were also determined.

3.2.3 Effect of reaction temperature and Ni loading. Fig. 5(a)–(d) illustrate the effect of reaction temperature and Ni loading on CH_4 conversion, CO and CO_2 selectivity, H_2 selectivity, and H_2/CO molar ratio during the POM reaction using N_2O. Fig. 6(a) reveals that the CH_4 conversion of the LSCF, 10% Ni/LSCF, and 20% Ni/LSCF catalysts increased from 20.1% to 99.3%, 70.9% to 99.6%, and 19.0% to 99.4%, respectively, as the temperature increased from 600 to 900 °C, indicating a higher reaction rate at elevated temperatures. The addition of 10% Ni to LSCF significantly enhanced CH_4 conversion within the temperature range of 600–850 °C, emphasizing the role of Ni as the active site for the POM reaction. However, increasing the Ni loading to 20% reduced CH_4 conversion, likely due to the

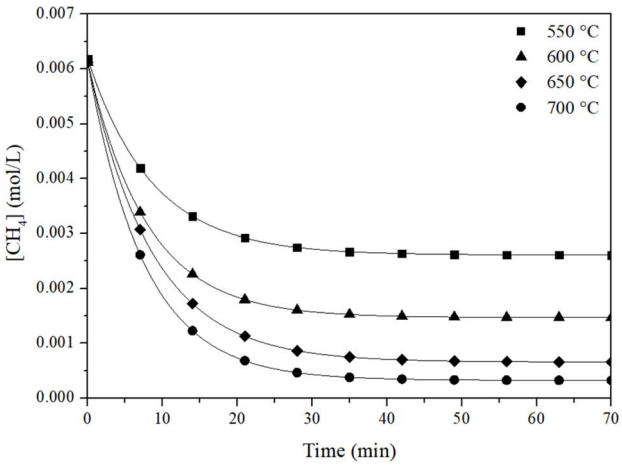

Fig. 6 The variation in CH_4 concentration as a function of time at different temperatures (550, 600, 650 and 700 °C) for the POM using N_2O over the 10% Ni/LSCF catalyst.

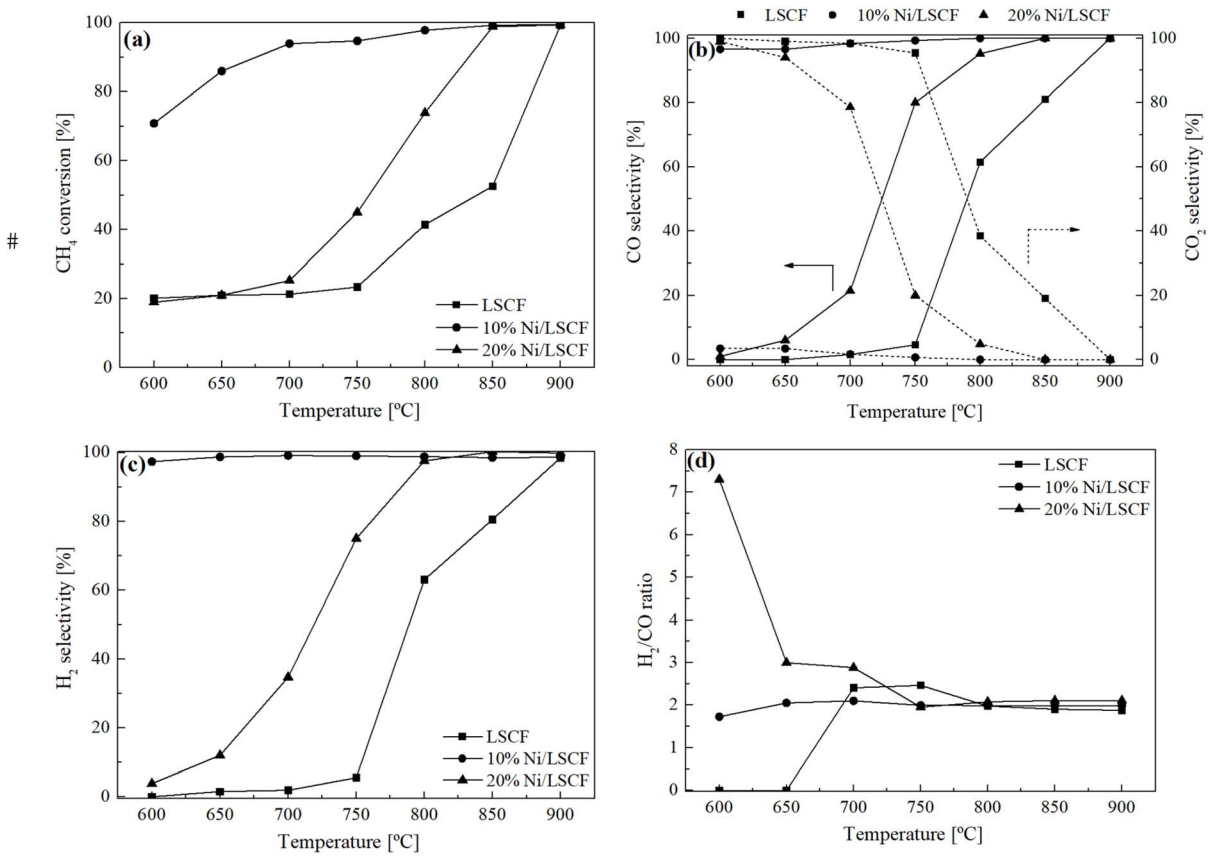

Fig. 5 Catalytic performances of Ni-doped LSCF with Ni content of 0, 10, and 20% in terms of (a) CH_4 conversion, (b) CO and CO_2 selectivity, (c) H_2 selectivity, and (d) ratio of H_2/CO as a function of temperature for the partial oxidation of CH_4 using N_2O ($CH_4 : N_2O = 1 : 1$, WHSV = 3000 mL g_{cat} h^{-1}, atmospheric pressure).

formation of a larger Ni crystallite size, which lowered the dispersion of Ni on the LSCF surface,[42] limited the complete reduction of NiO to metallic Ni, decreased the surface reactivity, and lowed the strength of metal–support interaction.

Fig. 5(b) and (c) show the selectivity of CO, CO_2, and H_2 for all LSCF-based catalysts as a function of temperatures. The 10% Ni/LSCF catalyst consistently exhibited the CO and H_2 selectivity during the entire temperature range (600–900 °C), with average values of 98.7% and 98.6%, respectively. At 600 °C, the LSCF catalyst exhibited 100% CO_2 selectivity, without the production of CO or H_2, likely due to the absence of active Ni species on its surface. In contrast, the 20% Ni/LSCF catalyst showed 98.9% CO_2 selectivity, with CO and H_2 selectivity values of 1.0% and 3.8%, respectively. This is likely attributed to the larger NiO crystallite size, as mentioned above. However, with increasing temperature, both LSCF and 20% Ni/LSCF catalysts revealed a decline in CO_2 selectivity, while enhanced CO and H_2 selectivity.

Fig. 5(d) illustrates the effect of Ni loading on the H_2/CO molar ratio as a function of reaction temperature. The 10% Ni/LSCF catalyst achieved an H_2/CO ratio of 2.0–2.1 between 650–900 °C. In contrast, the H_2/CO ratio for LSCF was zero within the 600–650 °C range, indicating no detectable formation of CO and H_2. At 700–750 °C for LSCF and 600–700 °C for 20% Ni/LSCF catalyst, the H_2/CO ratios exceeded 2, likely due to methane dissociation on Ni active sites and water–gas shift reaction (eqn (19)).[43] However, both catalysts achieved the optimal H_2/CO ratio of 2, corresponding to the POM reaction at higher temperatures.

$$CO + H_2O \rightarrow CO_2 + H_2,\ \Delta H_{298K} = -41.2\ \text{kJ mol}^{-1} \quad (19)$$

These results indicate that the size of active Ni species affects product selectivity and reaction pathways. It has been reported that the POM reaction proceeds *via* two distinct pathways: (i) an indirect pathway where CH_4 is completely combusted to CO_2 and H_2O at lower temperatures (eqn (20)), followed by dry (eqn (21)) and steam (eqn (22)) reforming of CH_4 to yield CO and H_2 at higher temperatures and (ii) a direct pathway where CH_4 is partially oxidized to directly produce CO and H_2 (eqn (23)). The 10% Ni/LSCF catalyst, with a smaller NiO crystallite size (23.7 nm) favours the direct pathway, as evidenced by the H_2/CO ratio of 2.0–2.1 during the entire temperature range, due to improved Ni dispersion and a larger interfacial area between the Ni metal and the support.[34] In contrast, both pure LSCF and the 20% Ni/LSCF catalyst, with larger NiO crystallite sizes (32.3 nm), proceed *via* the indirect pathway, as confirmed by the syngas production at higher temperatures. Furthermore, the indirect pathway may result in Ni sintering due to the exothermic nature of the complete CH_4 combustion, leading to rapid catalyst deactivation.[44]

$$CH_4 + 2O_2 \rightarrow CO_2 + 2H_2O,\ \Delta H_{298K} = -802.3\ \text{kJ mol}^{-1} \quad (20)$$

$$CH_4 + CO_2 \rightarrow 2CO + 2H_2,\ \Delta H_{298K} = +247\ \text{kJ mol}^{-1} \quad (21)$$

$$CH_4 + H_2O \rightarrow CO + 3H_2,\ \Delta H_{298K} = +206\ \text{kJ mol}^{-1} \quad (22)$$

$$CH_4 + 1/2O_2 \rightarrow CO + 2H_2,\ \Delta H_{298K} = -36\ \text{kJ mol}^{-1} \quad (23)$$

3.2.4 Kinetic measurement. Understanding the kinetics of chemical reactions is essential for optimizing processes and designing reactors. The kinetics of the POM reaction using N_2O for the 10% Ni/LSCF catalyst were examined at the temperature range from 550 to 700 °C. In this process, CH_4 is activated by the active oxygen species (O*) generated from the decomposition of N_2O as follows:

$$N_2O + * \rightarrow N_2 + O* \quad (24)$$

$$O* + CH_4 \rightarrow CO + 2H_2 + * \quad (25)$$

Fig. 6 illustrates the effects of temperature and time on CH_4 concentration during the reaction. The rate of the reaction ($-\mathrm{d}[CH_4]/\mathrm{d}t$) can be achieved from the slope of this plot. The initial rate increased with temperature due to higher kinetic energy and increased reaction collisions. The gaseous N_2O was not observed during the reaction, implying that eqn (24) is a very fast reaction. Therefore, reaction (25) has been postulated as the rate-determining step for the POM reaction using N_2O. When the catalyst weight was kept constant, the reaction rate is only dependent on the CH_4 concentration and the power rate law can be written as eqn (26), where $[CH_4]$ denotes the concentrations of CH_4. The parameter k represents the rate constant while m denotes the reaction order with respect to CH_4.

$$\text{Rate} = \frac{-\mathrm{d}[CH_4]}{\mathrm{d}t} = k \times [CH_4]^m \quad (26)$$

The reaction order (m) and the rate constant (k) can be determined using integrated rate equation. The result exhibited that the plot of inverse concentration of CH_4 ($1/[CH_4]$) as a function of time gives a straight line (R^2 = 0.986–0.9997), corresponding to the second order reaction. The rate constant can be also obtained from the slope of this plot with the values

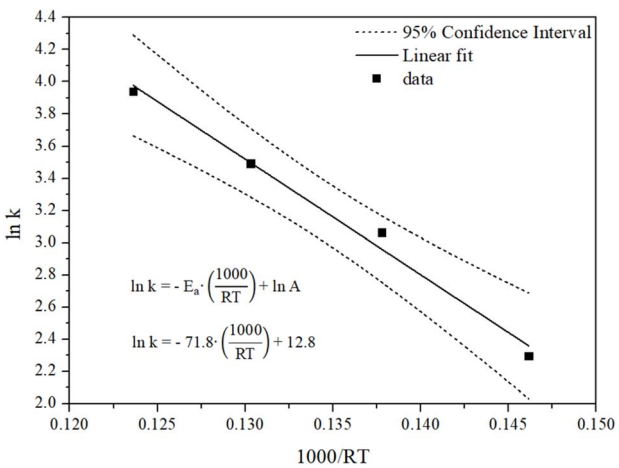

Fig. 7 The Arrhenius plot between ln k and $1000/RT$ for the POM using N_2O over the 10% Ni/LSCF catalyst at the temperature range of 550–700 °C.

of 9.94, 21.41, 32.92, and 51.52 L mol^{-1} min^{-1} for 550, 600, 650, and 700 °C, respectively. The activation energy (E_a) was calculated using the Arrhenius equation (eqn (27)) by plotting ln k against the reciprocal of absolute temperature (T), as illustrated in Fig. 7, where R is the gas constant (8.314 J mol^{-1} K^{-1}). The apparent activation energy (E_a) for the POM reaction using N_2O over the 10% Ni/LSCF catalyst was found to be 71.8 kJ mol^{-1}, consistent with previous research. T. Nakazato *et al.*[45] reported an activation energy of 71.3 kJ mol^{-1} for the POM reaction over a 5% Ni-doped hydroxyapatite composite catalyst. Similarly, R. K. Singha *et al.*[34] obtained an activation energy of 72.7 kJ mol^{-1} using a 5% Ni/CeO_2 catalyst.

$$\ln k = \ln A - \frac{E_a}{RT} \quad (27)$$

4. Conclusions

The addition of 10% Ni to LSCF enhanced the catalytic performance for both N_2O decomposition and POM reactions. While LSCF serves as a stable support and promotes oxygen mobility within the catalyst, the presence of Ni introduced active sites that facilitated these reactions, leading to excellent performance in N_2O decomposition, achieving complete decomposition to N_2 and O_2 at lower operating temperatures compared to the Ni-free catalyst. LSCF perovskites are known for their mixed ionic-electronic conductivity and oxygen mobility, combining them with Ni for N_2O decomposition and POM introduces a novel hybrid catalyst system. The synergy between the oxygen storage capacity of LSCF and the active metallic Ni sites for methane oxidation is a significant finding.

The addition of 10% Ni resulted in smaller Ni crystallite sizes (23.7 nm), improving Ni dispersion and increasing the active surface area compared to the larger crystallites formed with 20%Ni (32.3 nm). These smaller Ni particles facilitated the reduction of NiO to metallic Ni, which acts as the active site for the POM reaction. As a result, the 10% Ni/LSCF catalyst exhibited superior catalytic performance for POM using N_2O, achieving 70.9% CH_4 conversion, 96.6% CO selectivity, and 97.4% H_2 selectivity at a low temperature of 600 °C. In contrast, LSCF without Ni and the catalyst with 20% Ni loading showed significantly lower efficiency, with only around 20% CH_4 conversion and less than 5% syngas selectivity. Additionally, this study demonstrated that smaller Ni particles favoured the direct POM reaction pathway, leading to the formation of CO and H_2, whereas larger Ni particles promoted the indirect pathway, involving complete CH_4 combustion followed by reforming processes. The kinetic study revealed that the POM reaction using N_2O over the 10% Ni/LSCF catalyst followed second order kinetics with respect to CH_4 and was independent of N_2O, with an apparent activation energy of 71.8 kJ mol^{-1}. This suggests that the rate-limiting step likely involves the adsorption or activation energy of CH_4 on the catalyst surface. This could imply that the adsorption or activation of CH_4 on the catalyst surface is critical. Typically, in POM reactions, CH_4 dissociation is one of the slowest steps, supporting the conclusion that CH_4 activation is the rate-limiting process. The independence of the reaction rate from N_2O suggests that N_2O serves primarily as an oxygen donor in the reaction, and its concentration does not affect the overall reaction rate. The LSCF support's role in oxygen mobility is consistent with the observation that N_2O decomposition is not rate-limiting. LSCF perovskites are known for their high oxygen mobility, so the oxygen from N_2O can efficiently be transferred to CH_4-derived intermediates. This also suggests that the catalyst's structure, particularly LSCF's oxygen vacancy capabilities, supports efficient oxygen transfer without causing kinetic limitations. It can be concluded that the catalyst is suitable for the reaction as long as there is sufficient CH_4. Given that oxygen is readily supplied, improvements can be CH_4 activation enhancement or increasing the number of active Ni sites.

For future work, the Ni dispersion optimization (*e.g.* by improving impregnation method or adding additional metals oxides such as CeO_2 or ZrO_2 as stabilizers[46]) could be studied. High Ni loading tends to cause agglomeration. To overcome this, introducing a second metal (such as Cu or Co) can improve the dispersion of Ni and prevent sintering.[47] The bimetallic approach can also introduce synergistic effects, where the secondary metal aids CH_4 activation which could be enhanced by promoting oxygen mobility *i.e.* doping Ce and/or Mn[48,49] to improve the oxygen exchange for POM or creating more oxygen vacancies by synthesizing the perovskites under mild reducing conditions (create more defects). Additionally, electronic promoters such as alkali metals (K, Na)[50] can be used to modify the electronic properties of the active metal sites such as Ni or Cu, which facilitates easier activation of reactants such as CH_4.

Data availability

The data that support the findings of this study are available on request.

Conflicts of interest

There are no conflicts to declare.

Acknowledgements

This research has received funding support from the NRCT (contract number N41A640254 and N83A670023), King Mongkut's University of Technology North Bangkok (contract number KMUTNB-FF-66-52), and NSRF *via* the Program Management Unit for Human Resources & Institutional Development, Research and Innovation (contact number B48G660108).

References

1 T. J. Griffis, Z. Chen, J. M. Baker, J. D. Wood, D. B. Millet, X. Lee, R. T. Venterea and P. A. Turner, *Proc. Natl. Acad. Sci. U. S. A.*, 2017, **114**, 12081–12085.
2 Y. Shimizu, *Membrane*, 1990, **15**, 179–187.
3 M. Evans and V. Roshchanka, *Atmos. Environ.*, 2014, **92**, 199–206.

4 O. Badr, S. D. Probert and P. W. O'Callaghan, *Appl. Energy*, 1991, **40**, 273–313.
5 M. Konsolakis, *ACS Catal.*, 2015, **5**, 6397–6421.
6 Z. Zhuang, B. Guan, J. Chen, C. Zheng, J. Zhou, T. Su, Y. Chen, C. Zhu, X. Hu, S. Zhao, J. Guo, H. Dang, Y. Zhang, Y. Yuan, C. Yi, C. Xu, B. Xu, W. Zeng, Y. Li, K. Shi, Y. He, Z. Wei and Z. Huang, *Chem. Eng. J.*, 2024, **486**, 150374.
7 M. Galle, D. W. Agar and O. Watzenberger, *Chem. Eng. Sci.*, 2001, **56**, 1587–1595.
8 M. J. Rogoff and F. Screve, in *Waste-to-Energy*, 2011, pp. 89–116.
9 G. Centi and F. Vazzana, *Catal. Today*, 1999, **53**, 683–693.
10 V. A. Zakirov, V. Goeman, T. J. Lawrence and M. N. S, in, *Proceedings of the 14th Annual AIAA/USC Conference on Small Satellites*, 2000, SSC00-XI–6.
11 K. Q. Tran, P. Kilpinen and N. Kumar, *Appl. Catal., B*, 2008, **78**, 129–138.
12 N. A. Khan, E. M. Kennedy, B. Z. Dlugogorski, A. A. Adesina and M. Stockenhuber, *J. Energy Chem.*, 2017, **26**, 155–162.
13 X. Gao, Y. Li, J. Chen, X. Yang, Z. Zhang, Z. Chang and Y. Li, *Mol. Catal.*, 2021, **510**, 111713.
14 Z. Ou, Z. Zhang, C. Qin, H. Xia, T. Deng, J. Niu, J. Ran and C. Wu, *Sustain. Energy Fuels*, 2021, **5**, 1845–1856.
15 N. Richards, L. A. Parker, J. H. Carter, S. Pattisson, D. J. Morgan, N. F. Dummer, S. E. Golunski and G. Hutchings, *Catal. Lett.*, 2022, **152**, 213–226.
16 G. Sai Gautam, E. B. Stechel and E. A. Carter, *Chem. Mater.*, 2020, **32**, 9964–9982.
17 K. L. Pan, S. J. Yu, S. Y. Yan and M. B. Chang, *J. Air Waste Manage. Assoc.*, 2014, **64**, 1260–1269.
18 C. Huang, Y. Zhu, X. Wang, X. Liu, J. Wang and T. Zhang, *J. Catal.*, 2017, **347**, 9–20.
19 M. S. Santos, R. C. R. Neto, F. B. Noronha, P. Bargiela, M. G. C. Rocha, C. Resini, E. Carbó-Argibay, R. Fréty and S. T. Brandao, *Catal. Today*, 2018, **299**, 229–241.
20 A. Aliyatulmuna, R. Y. Perry Burhan, H. Fansuri and I. K. Murwani, *IOP Conf. Ser.:Mater. Sci. Eng.*, 2019, **515**, 9.
21 S. Rahayu, A. A. Fatah and G. M. Kale, *Energies*, 2021, **14**, 1800.
22 N. Li, A. Boréave, J. P. Deloume and F. Gaillard, *Solid State Ionics*, 2008, **179**, 1396–1400.
23 S. M. Babiniec, E. N. Coker, J. E. Miller and A. Ambrosini, *Sol. Energy*, 2015, **118**, 451–459.
24 S. D. Nurherdiana, N. Widiastuti, T. Gunawan, W. W. Lestari, R. R. Mukti and H. Fansuri, *Ceram.–Silik.*, 2022, **66**, 128–136.
25 K. Takehira, T. Shishido and M. Kondo, *J. Catal.*, 2002, **207**, 307–316.
26 X. Yin, R. Zhang, Y. Zhang, S. Wang and L. Shen, *Int. J. Hydrogen Energy*, 2024, **71**, 481–492.
27 J. Sunarso, S. Baumann, J. M. Serra, W. A. Meulenberg, S. Liu, Y. S. Lin and J. C. Diniz da Costa, *J. Membr. Sci.*, 2008, **320**, 13–41.
28 N. A. Abdullah, S. Hasan and N. Osman, *J. Chem.*, 2013, **2013**, 908340.
29 H. Kim, R. Mane, K. Han, H. Kim, C. Lee and Y. Jeon, *Nanomaterials*, 2022, **12**, 3325.
30 Y. Shi, C. Liu, J. Zhuo and Q. Yao, *ACS Omega*, 2020, **5**, 20299–20310.
31 J. Cihlar, R. Vrba, K. Castkova and J. Cihlar, *Int. J. Hydrogen Energy*, 2017, **42**, 19920–19934.
32 K. Zhao, A. Zheng, H. Li, F. He, Z. Huang, G. Wei, Y. Shen and Z. Zhao, *Appl. Catal., B*, 2017, **219**, 672–682.
33 S. Pavlova, L. Kapokova, R. Bunina, G. Alikina, N. Sazonova, T. Krieger, A. Ishchenko, V. Rogov, R. Gulyaev, V. Sadykov and C. Mirodatos, *Catal. Sci. Technol.*, 2012, **2**, 2099–2108.
34 R. K. Singha, A. Shukla, A. Yadav, L. N. Sivakumar Konathala and R. Bal, *Appl. Catal., B*, 2017, **202**, 473–488.
35 Y. Zheng, K. Li, H. Wang, D. Tian, Y. Wang, X. Zhu, Y. Wei, M. Zheng and Y. Luo, *Appl. Catal., B*, 2017, **202**, 51–63.
36 P. Pal, R. K. Singha, A. Saha, R. Bal and A. B. Panda, *J. Phys. Chem. C*, 2015, **119**, 13610–13618.
37 C. Khajonvittayakul, V. Tongnan, T. Kangsadan, N. Laosiripojana, S. Jindasuwan and U. W. Hartley, *React. Kinet., Mech. Catal.*, 2019, **127**, 839–855.
38 L. Xue, C. Zhang, H. He and Y. Teraoka, *Appl. Catal., B*, 2007, **75**, 167–174.
39 U. W. Hartley, V. Tongnan, N. Laosiripojana, P. Kim-Lohsoontorn and K. Li, *React. Kinet., Mech. Catal.*, 2018, **125**, 85–97.
40 G. Whittingham, *Nature*, 1947, **159**, 232.
41 M. Shelef and G. W. Graham, *Catal. Rev.:Sci. Eng.*, 1994, 433–457.
42 M. Peymani, S. M. Alavi and M. Rezaei, *Int. J. Hydrogen Energy*, 2016, **41**, 6316–6325.
43 S. Eriksson, S. Rojas, M. Boutonnet and J. L. G. Fierro, *Appl. Catal., A*, 2007, **326**, 8–16.
44 X. Dai, C. Yu, R. Li, Q. Wu, K. Shi and Z. J. Hao, *Rare Earths*, 2008, **26**, 341–346.
45 T. Nakazato and T. Kai, *Chem. Eng. J. Adv.*, 2022, **9**, 100210.
46 R. Dziembaj, M. Molenda and L. Chmielarz, *Catalysts*, 2023, **13**.
47 X. Yu, F. Zhang and W. Chu, *RSC Adv.*, 2016, **6**, 70537–70546.
48 M. Boaro, S. Colussi and A. Trovarelli, *Front. Chem.*, 2019, **7**, 28.
49 M. Chen and L. Wang, *Catalysts*, 2024, **14**, 355.
50 M. N. Younis, Z. Ren, C. Li, E. Wang and J. Li, *Catalysts*, 2023, **13**, 450.